

A study on the efficacy of flow mitigation devices in
hard disk drives

Sujit Kirpekar and David B. Bogy

Computer Mechanics Laboratory

Department of Mechanical Engineering

University of California at Berkeley

Berkeley, CA 94720

`kirpekar@newton.berkeley.edu`

April 7, 2005

Contents

1 Part (1)	3
1.1 Prior Research	3
1.1.1 Experimental research	3
1.1.2 Numerical research	5
1.2 Model Setup	6
2 Part (2)	7
2.1 Major Flow Features	7
2.2 Evolution of flow	9
2.3 Turbulence intensity	11
2.4 Pressure distribution on disks	12
3 Part (3)	13
3.1 Velocity fluctuations	13
3.2 Pressure difference across the actuator	15
3.3 Windage	16
4 Conclusions	17
5 Tables	23
6 Figures	26

List of Figures

1	Top view of M0 geometry: original simulation	26
2	Top view of M1 geometry: blocking plate	26
3	Top view of M2 geometry: downstream spoiler	26
4	Top view of M3 geometry: upstream spoiler	26
5	M0: Snapshot of turbulent field in the drive. Plot of axial velocity component on the midplane	27
6	M1: Snapshot of turbulent field in the drive. Plot of axial velocity component on the midplane	27
7	M2: Snapshot of turbulent field in the drive. Plot of axial velocity component on the midplane	27
8	M3: Snapshot of turbulent field in the drive. Plot of axial velocity component on the midplane	27
9	Inter-disk azimuthal velocity profile, at 340° from origin, i.e. in the wake . . .	28
10	Inter-disk azimuthal velocity profile, at 45° from origin	28
11	Inter-disk azimuthal velocity profile, at 135° from origin	28
12	Inter-disk azimuthal velocity profile, at 225° from origin	28
13	Inter-disk radial velocity profile, at 340° from origin, i.e. in the wake	29
14	Inter-disk radial velocity profile, at 45° from origin	29
15	Inter-disk radial velocity profile, at 135° from origin	29
16	Inter-disk radial velocity profile, at 225° from origin	29
17	Chord locations for calculation of turbulence intensity	30
18	Turbulence Intensity along chord 1	31
19	Turbulence Intensity along chord 2	31
20	Turbulence Intensity along chord 3	31

21	Turbulence Intensity along chord 4	31
22	M0: Contours of the instantaneous pressure field acting on the top disk . . .	32
23	M1: Contours of the instantaneous pressure field acting on the top disk . . .	32
24	M2: Contours of the instantaneous pressure field acting on the top disk . . .	32
25	M3: Contours of the instantaneous pressure field acting on the top disk . . .	32
26	Location of points along actuator face for which velocity and pressure data is reported	33
27	RMS fluctuation in-plane velocity fluctuations	34
28	M0: Frequency Spectra of in-plane velocity fluctuations for data points 1-32	35
29	M1: Frequency Spectra of in-plane velocity fluctuations for data points 1-32	35
30	M2: Frequency Spectra of in-plane velocity fluctuations for data points 1-32	36
31	M3: Frequency Spectra of in-plane velocity fluctuations for data points 1-32	36
32	RMS fluctuation out-of-plane velocity fluctuations	37
33	M0: Frequency Spectra of out-of-plane velocity fluctuations for data points 1-32	38
34	M1: Frequency Spectra of out-of-plane velocity fluctuations for data points 1-32	38
35	M2: Frequency Spectra of out-of-plane velocity fluctuations for data points 1-32	39
36	M3: Frequency Spectra of out-of-plane velocity fluctuations for data points 1-32	39
37	RMS fluctuations of Pressure	40
38	M0: Frequency Spectra of pressure fluctuations for data points 1-32	41
39	M1: Frequency Spectra of pressure fluctuations for data points 1-32	41
40	M2: Frequency Spectra of pressure fluctuations for data points 1-32	42
41	M3: Frequency Spectra of pressure fluctuations for data points 1-32	42
42	Windage loss at disks	43

List of Tables

1	Geometry data	23
2	Model specific geometry data, M1	23
3	Model specific geometry data, M2	23
4	Model specific geometry data, M3	24
5	CFD modeling information	24
6	Boundary conditions	24
7	Grid information	24
8	Common Legend for Figures in the paper	25

Abstract

Large eddy simulations of the turbulent flow of air in hard disk drives (HDD) are reported using a commercial CFD code. In particular, HDD casings which claim reduction in flow induced vibrations by the use of small geometrical modifications are investigated. The modifications investigated are: M1: a blocking plate situated between the disks, M2: a spoiler (or deflector) located behind (downstream of) the actuator arm and M3: a similar deflector upstream of the arm. This paper is primarily concerned with the Fluid Mechanics of flows with such devices. It is observed that M1, M2 and M3 significantly modify the mean flow patterns in the drives. M1 reduces velocity magnitudes in most parts of the drive, the modification of M2 causes flow reversal in regions close to the hub, while M3 causes the shedding of vortices upstream of the actuator arm. Our analysis points to M1 as the best candidate for mitigating the effects of turbulent airflow. This is because, M1 is more effective than M2 and M3 in reducing the RMS of velocity fluctuations near the suspension. M1 is also more effective in reducing the pressure fluctuations near the base-plate and suspension region. This improvement in reduced fluctuations, however, is at the cost of approximately 20% higher windage. Finally, it is also noted that M3 has the adverse effects of increasing velocity and pressure fluctuations and hence is the worst candidate for mitigating airflow effects.

Introduction

The turbulent flow of air generated by spinning disks in hard disk drives (HDD) is known to be major contributor to undesirable vibrations of the head stack assembly (HSA). The continuing demand for higher capacities in HDD has resulted in a continual increase in areal densities. Densities in excess of 100 Gb/in² have been demonstrated and it is widely projected that conventional technology will ultimately achieve 1 Tb/in². It is foreseeable that

at such areal densities, a track density of 0.5 Million tracks/inch will be required, with each recorded bit being roughly 13 x 50 nm [27]. Under such conditions, the tracking accuracy required is approximately 1.5 nm RMS (root mean square). These goals place stringent requirements on the positioning accuracy of the actuator while accentuating the need to mitigate the various sources of track misregistration (TMR).

Several methods / techniques have been proposed to tackle the TMR problem:

1. By reducing the disk diameter and increasing its thickness, which increases the rigidity of the disk, reducing TMR caused by disk flutter and spindle run-out
2. By increasing the stiffness of the HSA, especially the suspension. This causes the modes of vibration to move to higher frequency ranges, thereby reducing their relative amplitudes
3. By achieving better control using a dual stage actuator
4. By isolating the drive from external vibration, using fluid spindle bearings and possibly replacing the air with a lower density, non-corrosive gas like Helium [27]
5. By modifying the air flow in the drive using geometrical features, such that the resultant HSA vibrations are reduced

The goal of this work is to study the effect of several flow mitigation devices that are commonly used in disk drive casings. These modifications are in current use in disk drives and have been selected for investigation after examining several disk drives available in the market, in late 2004. The modifications investigated are: M1: a blocking plate situated between the disks, M2: a spoiler (or deflector) located behind (downstream of) the actuator arm and M3: a similar deflector upstream of the arm. A comparison is made between the modifications M1-3 and the original disk drive without any modification, which we denote as M0.

This paper is organized into three parts:

1. In part (1) we review the literature on the problem of air flow effects in disk drives, both experimental and numerical. Next we describe the geometric details of the modifications and outline the simulation techniques we used.
2. In part (2) we discuss the major flow features associated with each modification with a view to understand the underlying physics. We report on how the flow develops after formation of the wake and how the turbulence intensity varies across the drive enclosure.
3. In part (3) we present velocities and pressure data in the immediate vicinity of the actuator arm. Here we present RMS fluctuations and their corresponding frequency content.

1 Part (1)

1.1 Prior Research

There has been significant experimental, theoretical and numerical research on air flow in hard disk drives, over the past 30 years. We attempt to present a summary of the main accomplishments so far.

1.1.1 Experimental research

The experimental work of Lennemann [13] was one of the first experimental investigations directly focused on disk drives. The author used model disks of diameter between 355.6 - 457 mm running at 710-3600 rpm and used water and aluminum powder for flow visualization. Experiments were performed with and without a slider arm. The author shows the existence of a central laminar core that is rotating slightly slower than the disk and a highly turbulent

outer region. The paper also contains an extensive list of prior work related to rotating disks, but not specifically disk drives.

Kaneko *et al.* [9] performed similar flow visualization experiments to study the flow between disks with and without a cylindrical shroud. They observed a “bumpy laminar core” that extended from the hub to the mid-radius of the disks, followed by a “more turbulent outer region”

Abrahamson *et al.* [1] performed experiments using an acid-base indicator, Bromothymol Blue, in water. Disk speeds were varied from 5-50 rpm, the disk diameter was fixed at 112 cm. They observed three distinct regions of flow: “a solid body inner region near the hub, an outer region dominated by counter rotating vortices and a boundary layer region near the shroud”. They reported that decreasing the Ekman number ($Ek = \nu/R^2\Omega$) or increasing the axial spacing between the disks resulted in lesser vortical structures in the outer region and consequently greater overall mixing.

Girard *et al.* [4] investigated the effect of an actuator-like rotary arm on the flow field in the drive, using water based flow visualization. Their main conclusions were related to the effect of the arm and the wake it creates.

Tzeng *et al.* [24], Schuler *et al.* [17] and Usry *et al.* [25] performed several laser-Doppler velocimetry experiments of rotating disks with and without an obstruction. They primarily reported mean and RMS values of circumferential velocities and the corresponding frequency content. Usry *et al.* [25] also conclude that once the flow separates by flowing over the obstruction, “the flow does not recover within one revolution from the effects of the obstruction”.

Experimental research using realistic disk drive configurations for suspensions and sliders has been limited. Yamaguchi *et al.* [28] performed hot wire anemometer experiments using a suspension in a uniform and rotating flow. They found no noticeable peaks in the frequency content of the flow and concluded that the flow acts as an aperiodic irregular excitation.

In the recent work by Gross [5], experimental data in the near vicinity of the e-block arm was made available. Gross also investigated the effect of the thickness of the e-block arm and the shape of its trailing edge on the airflow and consequently on the flow induced vibrations in the slider.

1.1.2 Numerical research

Among the first numerical investigations of the air flow in disk drive like enclosures was done by Chang *et al.* [2]. Using a finite difference code incorporating the $k-\epsilon$ model, they showed good agreement between experiments and simulation with regard to the mean flow velocity and heat transfer characteristics.

The first three-dimensional numerical study of the *unsteady* flow was published by Humphrey *et al.* [7]. They showed that the toroidal vortices at the shroud “acquire a time-varying sinusoidal shape in the circumferential direction”.

Using a different code, Suzuki *et al.* [21] numerically studied the effect of a radially inserted actuator arm and an “airlock” (which is a similar obstruction to the flow). They mainly discuss the pressure, shear stress and disk torque coefficient that they compute. Using the same code as [21] Iglesias *et al.* [8] performed 2- and 3-dimensional calculations for different Reynolds numbers. Using a similar non-commercial software Kazemi [10] has conducted 2-D and 3-D numerical calculations of the flow around a suspension-head unit and reports the resulting vibrations calculated by a finite element technique.

Most of the recent works on air flows in disk drives have used commercial CFD software. Due to the rapid increase in computer speeds and research advances in turbulence modeling, numerical investigations are increasingly modeling the geometrical complexities of a real HDD.

Ng *et al.* [16] performed CFD calculations using CFX-5, Shimizu *et al.* [19] used large eddy simulation (LES) to study flow induced disk flutter, and in [18] Shimizu *et al.* used LES

to study the airflow induced vibrations of the HGA. Tsuda *et al.* [23] report DNS results, while Tatewaki *et al.* [22] report LES results of airflows in realistic disk drives.

Recognizing that the air flow in a disk drive is highly unsteady and random, most researchers have performed unsteady (time-marching) calculations, typically using LES, (or where resources permit, DNS). Calculations based on Reynolds Averaged methods (which are useful in predicting mean flow fields and particle trajectories) have also been reported by Song *et al.* [20]

Finally, there has also been some published work on reducing flow induced vibrations in disk drives. Hirono *et al.* [6] study the effect of an upstream spoiler, while Nakamura *et al.* [15] study the effect of miniaturizing the suspension.

1.2 Model Setup

A top view of the geometrical models simulated are shown as follows, M0 in Figure 1, M1 in Figure 2, M2 in Figure 3 and M3 in Figure 4. The relevant geometrical modifications have been highlighted for clarity. Geometrical data that is common to all simulations is given in Table 1, while geometrical data specific to each simulation is given in Tables 2-4. Numerical modeling information that is common to all simulations is given in Table 5 and boundary conditions are outlined in Table 6. Our simulations use the Algebraic dynamic LES model [3] which we consider to be the optimal LES model for the current work (see [11]). To avoid the well known diffusive behavior of upwind based methods with LES [14], we use central differencing for discretizing the convective terms. A time step of 2×10^{-5} seconds was chosen so that we are able to resolve a maximum frequency of 25 kHz. A steady $k - \epsilon$ solution was used as initial conditions for all of the simulations. Such a steady $k - \epsilon$ solution forms a good equilibrium approximation to the mean flow from which the transient solutions can be computed.

Finally, information about the mesh used in the simulations is given in Table 7. All

simulations used an unstructured mesh that was created in 2-D and extruded in the axial direction. The mesh generation algorithm creates a grid which is dominant in quadrilateral cells, with approximately 90% of the cells being quadrilateral, the rest being triangular. This helps in two ways: more grid lines (i.e. cell faces) can be oriented orthogonal to the direction of the mean flow, and the total number of cells for a given maximum cell width is reduced, compared with a purely triangular mesh.

In Table 7 the average cell volume is calculated by taking a mean of all the computational volumes in the simulation domain. The average grid resolution is the cube root of the average cell volume, which forms a measure of the representative grid size.

2 Part (2)

We start by discussing some physical features of the flow and subsequently describe the more quantitative results.

2.1 Major Flow Features

Flows in disk drive enclosures are highly unsteady with partly laminar and partly turbulent regions. Snapshots of the turbulent flow in our simulations are shown in the Figures 5 - 8. Plotted therein is the axial component of velocity on the midplane between the disks. Instead of choosing a monotonic scale for plotting this component of velocity, a staggered scale (similar to an interference pattern) is used. This helps in visualizing sharp velocity gradients that characterize the turbulent eddies, which may not appear in a monotonic scale. However quantitative information about the velocity magnitude is lost in this presentation mode. Nonetheless, this is acceptable for now, since we refer to quantitative data in later sections.

As the air flows over the structures forming an obstruction, it undergoes separation

causing the formation of vortical structures (see (1) in Figure 5). The vortex shedding causes changes in the circulation around the arm, which causes fluctuation in the drag it experiences. Turbulent eddies formed in the wake of the arm are convected by the mean flow due to the disk rotation and dissipate by the time they reach an angular position of approximately 225° ¹ (see (2) in Figure 5). The turbulence intensity of the flow coming towards the actuator arm is between 5-10% (as later explained by Figure 18). At the curved wall which forms the shroud one observes the presence of one or two toroidal vortices (see (3) in Figure 5). These structures are Göertler-type vortices formed due to three dimensional instability of the laminar boundary layer as it flows over the concave boundary. Finally, in the region upstream of the actuator arm, where the enclosure expands to accommodate the arm, one observes the separation of the flow and the formation of a turbulent region. (see (4) in Figure 5)

When compared with M0, M1 shows significant changes in the flow field, which is plotted in Figure 6. The presence of the blocking plate essentially blocks out a significant portion of the flow, forcing the rest around it. The mean velocity of the flow is reduced because the blocking plate acts in regions where the linear velocity of the disk is higher. However, eddy shedding at the trailing edge of the blocking plate increases the turbulence of the flow approaching the e-block arm (see (5) in Figure 6). Also, one observes the presence of a region of flow reversal (and stagnation) near the hub. The presence of the blocking plate causes an adverse pressure gradient in the air flowing towards it, causing some portions of the flow to stagnate and reverse direction (see (6) in Figure 6).

In simulation M2, plotted in Figure 7, the presence of a thick (1.6 mm compared to a disk-to-disk spacing of 2.2 mm) downstream rib blocks a significant portion of the flow. At the midplane, the mean azimuthal velocity is decreased almost everywhere in the drive. The

¹In describing radial and angular locations of our geometry, the origin is taken at the center of rotation of the disks. Angular positions are calculated by counter-clockwise rotation from the horizontal axis

presence of the rib causes the flow to stagnate and reverse direction in a significant portion of the drive (see (7) in Figure 7). The rib is a source of eddy shedding too, which increases the turbulence intensity of the downstream flow (see (8) in Figure 7).

In simulation M3, which is plotted in Figure 8, the flow field is similar to M0, except that the upstream spoiler acts as another source of generation of turbulent eddies. The eddies shed from the top and bottom edges cause added velocity fluctuations in the upstream portion of the flow field (see (9) in Figure 8). This significantly increases the velocity fluctuations near base of the e-block arm and the suspension.

2.2 Evolution of flow

It is expected that the airflow velocity magnitude is the smallest in the wake, and the flow gains momentum from the rotating disks as it flows around. To gain more insight into this process we plot the inter-disk velocity profiles at 4 points in the drive. In polar (r (mm), ϕ) coordinates, these 4 points are $(14.96, 340^\circ)$, $(14.96, 45^\circ)$, $(14.96, 135^\circ)$, $(14.96, 225^\circ)$. $r = 14.96\text{mm}$ corresponds to $1/3^{\text{rd}}$ the radial span of the disks, chosen so as to not lie within the blocking plate. The angular positions were chosen so as to not lie in the path of any modification. Data plotted in each figure is the average velocity profile over 6 revolutions of the disks. In this paper, when a direct comparison between simulations is permitted, the results are plotted using a common convention. This convention is explained in the legend given in Table 8.

In Figures 9 - 12 the azimuthal velocity of the flow is plotted as a function of the axial z coordinate for the above mentioned 4 points. $z = 0$ refers to the top of the bottom disk, while $z = 2.2\text{mm}$ refers to the bottom of the top disk. All figures are plotted to the same scale for convenience.

It is observed that, at 340° , in the wake, M0 shows the *fullest* profile, implying that the unmodified flow is the fastest in the wake. The velocity profile for M1 is less *full* because

of the presence of the blocking plate, while M2 shows a mid span flow reversal in the wake. The presence of the downstream rib and its corresponding pressure gradient causes the flow to reverse directions in the wake. Part of the flow closer to the disks flows in the direction of rotation, while the bulk of the center section flows in the reverse direction.

As the flow moves on to 45° , the velocity profiles for all the simulations become *fuller* due to the diffusion of momentum from the rotating disks. M0, which is the flow without any obstructions, shows the largest magnitude, while M2 shows the smallest profile. None of the profiles show flow reversal. The width of the (laminar) boundary layer is approximately the same in each simulation. M2 shows the largest velocity gradient in the boundary layer.

At 135° , M0 again shows the fullest profile, and M2 begins to show flow reversal, which is due to the presence of the downstream spoiler, approximately 180° upstream. The profile for M3 is similar to M0, reduced in magnitude by approximately 50%. This is a direct consequence of the upstream spoiler.

Finally at 225° , the profiles for M0 and M1 are almost identical, M3 is reduced from M0 by approximately 50%, while M2 shows flow reversal. This confirms the fact that the presence of the downstream spoiler causes a significant portion of the flow in the drive to reverse direction, mostly in the regions close to the hub.

As an aside, it is interesting to note that almost all the *mean* velocity profiles plotted in Figures 9 - 12 satisfy Fjørtoft's criteria for instability, which asserts that a necessary condition for instability of inviscid parallel flows is that $U_{yy}(U - U_I) < 0$ somewhere in the flow, where U_I is the velocity at the point of inflection of the profile. (For Fjørtoft's Theorem see [12]). This indicates that the mean flow profile in a disk drive enclosure (with or without the modifications) does satisfy the necessary condition for being linearly unstable in the inviscid limit. The only profiles that are stable are M0 and M3, both at 135° .

Figures 13-16 show the radial velocity as a function of the axial coordinate for the same 4 points as in Figures 9 - 12. In each Figure one observes a positive spike in radial velocity

immediately adjacent to the disks, as expected, due to the centrifugal effect.

At 340° , in the wake, the radial velocity profiles are not too different from each other. They are mainly affected by the constraining geometry of the model, which tends to squeeze the flow in the radial space between the hub and the shroud. For this reason, two peaks in the radial inflow velocity (i.e. negative radial velocity) are observed for each profile.

At 45° , the radial velocity of M1 is strongly negative. This is because the blocking plate tends to bend the streamlines towards the hub. The other profiles show radial outflow, with M2 showing the largest variation across the inter-disk spacing.

At 135° , M1 again shows the effect of the blocking plate, while M3 shows the effect of the upstream spoiler, both of which tend to create radial inflows.

Finally, at 225° , the presence of the upstream spoiler is clearly evident as indicated by the strong negative radial velocity profile for M3. On the other hand, M1 now shows larger positive radial velocity, since beyond the trailing edge of the blocking plate lies an expansion region where the flow can radially spread, before approaching the actuator.

2.3 Turbulence intensity

Figure 17 shows a schematic diagram of the disk drive enclosure with all three modifications super-imposed. Also shown in this figure are 4 chords running from the inner radius to the outer radius at angular positions of 340° : Chord 1; 45° : Chord 2; 135° : Chord 3 and 225° : Chord 4. Plotted in Figures 18 - 21 are the turbulence intensity (TI) profiles along these chords. The chord length is non-dimensionalized by the radial span of the disks. Turbulence intensity is defined as the ratio of the RMS of (total) velocity fluctuation to the mean velocity at that location. In general, one observes that the TI is higher in regions closer to the hub, than regions near the outer radius. This is because, near the hub, the disk velocities are small, the flow tends to reverse direction and hence the RMS fluctuations appear to be a larger fraction of the mean.

For chord 1 in Figure 18 one can clearly observe a single peak in TI due to the wake of the actuator arm for M0, M1 and M3. TI values are smaller near the outer and inner radii, hence it appears that a large part of the wake fluctuation is located near midway between the outer and inner radii. Compared to M0, M1 shows significantly reduced turbulence intensity. For M2 one observes two peaks, which is due to the vortex shedding occurring from the top and bottom edges of the downstream spoiler.

M1 shows higher fluctuations in Figures 19- 21 in regions adjacent to the hub. (In Figure 20 the TI profile for M1 is incomplete due to the blocking plate).

M0 and M3 show remarkably similar TI profiles along each chord, indicating the presence of the upstream spoiler does not change the turbulent fluctuations along the chords being considered.

2.4 Pressure distribution on disks

Plotted in Figures 22 - 25 are instantaneous contours of the pressure distribution on the top disk for M0-M3. In Figure 22, for M0, one observes that the pressure on the disk is uniform, showing clearly a radial pressure gradient. This radial uniformity is broken near the actuator. There is a high pressure region upstream of the arm, while the wake exerts lower pressures on the disk, as expected.

Comparing this to M1, in Figure 23, one observes that there is a build up of high pressure upstream of the blocking plate, and close to the hub the pressure is lower, which causes the flow to accelerate.

The downstream spoiler in Figure 24 causes a very sharp pressure gradient across it, which indicates that the flow is highly accelerated when flowing over (and under) the downstream spoiler. However, the pressure in the rest of the flow domain is nearly constant which is why the flow has a tendency to stagnate and recirculate.

The upstream spoiler in Figure 25 similarly causes a sharp pressure gradient across it

also, but the rest of the flow field is not altered significantly.

3 Part (3)

We now shift our attention from examining the entire flow domain to examining the region close to the actuator arm. The following results pertain to velocity and pressure data at a few specific points (ranging from 1-32), which are shown in Figure 26. These points lie close to the face of the actuator at an axial position which is at the center of the solid structure. E.g. points 4-10 are along the centerline of the e-block arm, while 12-22 are along the centerline of the lower suspension. We also note that the frequency spectra reported here using our LES cannot account for the spectra associated with the small scales of motion. LES solves for the large scales by taking into account the energy transfer mechanism between the large and the small scales of motion. However, since there is no explicit representation of the small scales, their contribution to the frequency spectra cannot be obtained.

3.1 Velocity fluctuations

To begin we examine the RMS of the in-plane ² velocity fluctuations. This is plotted in Figure 27. RMS fluctuations for M0-M3 have been plotted on separate figures for clarity.

The figure for M0 shows two distinct peaks near points 5-8. These are the fluctuations arising due to the expansion of the shroud just upstream of the e-block arm (See (4) in Figure 5). Two more peaks in fluctuation are observed: at point 18, due to the eddy shedding at the slider and at points 21-22, due to the eddy shedding from the corner of the base plate.

Comparing this to M1 it appears that M1 is able to dampen the fluctuations near the slider, but the fluctuations near the e-block arm actually increase. This is indeed a favorable

²In-plane refers to the plane of the disks

effect since fluctuations near the e-block arm contribute less to actuator vibrations than fluctuations near the slider. The added fluctuations near the e-block arm are due to the eddy shedding from the edge of the base plate (See (5) in Figure 6).

M2 displays less fluctuations near the base of the actuator but increased fluctuations near the region of the slider. Finally, M3 shows much higher fluctuations at the base of the actuator (points 1-5 and 29-32) and the base-plate and suspension region (points 10-15) due to the shedding of vortices from the upstream spoiler.

Further insight into the RMS fluctuations can be gained from the frequency spectra of the in-plane velocity at each point. This is plotted for M0-M3 in Figures 28 - 31. The coloration of each figure corresponds to dB amplitude of the spectrum.

Comparing Figure 29 to Figure 28 one readily observes that the blocking plate dampens the power in the spectrum at all locations except the base of the e-block arm. However, the spectra do not show significant changes near the suspension using any other modification. In fact, from Figure 31, it is evident that the presence of the upstream spoiler actually increases the fluctuations surrounding the actuator, especially near the base of the actuator and the leading edge of the suspension.

Plotted in Figure 32 are the RMS of the out-of-plane (axial) velocity fluctuations. The plot for M0 shows two significant peaks – one corresponding to the fluctuations arising from the expansion of the shroud, and the other corresponding to the eddy shedding off the slider edge. The trailing edge of the e-block arm (region 24-30) also shows higher axial fluctuations.

In the same figure, one observes that the out-of-plane fluctuations near the slider are reduced by the presence of the blocking plate, they are favorably reduced almost everywhere in M2, but are significantly increased in M3. The upstream spoiler contributes to the significantly high out-of-plane fluctuations near the base of the e-block arm (region 2-5 and 29-32).

Plotted in Figures 33 - 36 are the corresponding frequency spectra, which provide more

quantitative information regarding the out-of-plane velocity fluctuations. Again the spectrum for M1 in Figure 34 contains significantly lesser power than the spectrum for M0. A common observation from these figures is that, when a modification is used to reduce RMS fluctuations of velocity, higher frequency bands, corresponding to smaller eddies, are damped out. This implies that the energy content of the smaller eddies is reduced by the use of modifications like the blocking plate, while the energy content of the larger eddies, which is determined by the disk spacing and disk speed of rotation, remain relatively unchanged.

3.2 Pressure difference across the actuator

For hard disk drive actuators it is known that *form drag* due to pressure produces forces 2 orders higher in magnitude than *skin friction* (viscous) drag. Hence we examine the RMS of pressure fluctuations along the length of the actuator. Fluctuations in pressure at the leading or trailing face of the actuator contribute to its in-plane motions, while the lesser important out-of-plane pressure fluctuations acting on the top and bottom surfaces of the actuator cause bending in the suspension and e-block arm. We report only the in-plane pressure fluctuations.

Figure 37 is a plot of the RMS of pressure fluctuation for points 1-32. M0 shows two peaks in the RMS pressure fluctuation, the first due to the eddy separation due to the shroud expansion, while the next is due to the eddy shedding from the slider. M1 is effective in reducing the pressure fluctuations due to the eddy shedding from the corner of the base plate. M2 shows much smaller fluctuations near the base of the arm, but the fluctuations are increased near the suspension and base plates. No clear peaks in RMS are observed. Finally, M3 shows significantly larger fluctuations at the base of the actuator and at the location where the turbulent eddies shed from the upstream spoiler impinge on the suspension.

Figures 38 - 41 show the frequency spectra of the pressure fluctuations for M0-3. When compared to M0, M1 shows reduced frequency content in the higher frequency bands, indi-

cating that smaller eddies (i.e. eddies of higher frequencies) contribute less to the pressure fluctuations. This is especially important in the region of the suspension (between 14-22). Figure 40 shows that with the addition of a downstream spoiler, the frequency content of the spectrum is relatively unchanged, except that the amplitude of the spectrum is overall reduced. This suggests that although the amount of energy in pressure fluctuations has been reduced, the distribution of energy over spatial scales of motion has remained unchanged. Finally, Figure 41 confirms the fact that the upstream spoiler is ineffective in reducing pressure fluctuations.

3.3 Windage

It is expected that the cost of using modifications such as M0-3 should not be prohibitively high. Here we report on the *windage loss* calculated as a part of our simulations. Windage³ is calculated by integrating the shear stress over the disks to determine the power consumed (due to viscous action) by rotating the disks. Windage also represents the total energy input into our computational domain, while the sinks of energy are represented by molecular and sub-grid scale dissipation. Note that our calculations include the viscous loss at the hub, but do not include the viscous loss at the edge (rim) of the disks. It is expected that windage (i.e energy input) should remain constant over the duration of the simulation. Plotted in Figure 42 is the time history of the windage calculated as a function of the disk revolutions. One observes that although the initial conditions were inaccurate in predicting the windage, it asymptotes to a constant value in approximately 2 disk revolutions.

One also observes that M1, due to its large blocking plate, consumes the most power, while the windage loss for M2 is also high, given the flow reversal near the hub. This is expected given that the axial velocity gradients are considerably higher for M1 and M2 compared to M0 and M3 leading to higher shear stresses on the disks. The windage losses

³See [11] for discrepancies in the use of the term “windage”

for M0 and M3 are almost identical.

4 Conclusions

Numerical simulations have revealed several general insights into the flows inside disk drive casings. As the air flows over the actuator it separates at the leading edge corners which is a known point. The shear layer formed as a result of this rolls up into vortices which form the wake. The vortex shedding process is devoid of any coherency; it appears to be random as has been confirmed by several other researchers. The turbulent wake is transported by the mean flow of the rotating disks, while is dissipates by viscous action. Additional generation of vorticity takes place at the shroud, where toroidal vortices roll up due to the curvature of the streamlines. The use of the modifications discussed above generally result in additional points of eddy shedding, and depending on where the turbulence intensity is increased in the drive, this additional turbulence may or may not affect the actuator arm. On the other hand, M1 and M2 actually decrease the mean velocity of the flow as is demonstrated in the axial velocity profiles. This reduction in the kinetic energy of the flow (for the same disk rotation speed), causes reduced velocity fluctuations in the wake and in the regions immediately close to the actuator arm. Reiterating, in close proximity to the actuator arm, especially in the region of the base-plate and suspension (See points #11-23 in Figure 26) M1 has the smallest RMS in-plane and out-of-plane velocity fluctuations. M1 and M2 also have the smallest pressure fluctuations in this region while M3 appears to be a bad candidate based on all the RMS data presented.

We note that pressure-based loading on the actuator accounts for most of the off-track vibrations since pressure drag is 2 orders in magnitude larger than viscous drag. From this metric both M1 and M2 appear to be suitable candidates for reducing flow induced vibrations. However, we note that velocity fluctuations are also responsible for fluctuation

of the forces on the actuator, and their effect may not appear directly in the RMS of the pressure fluctuations, which is a second order statistical moment. Changes in the velocity field near the arm causes changes in circulation around the arm, which is linearly related to the loading on the actuator arm. (For the Kutta-Zhukowski theorem, see [12]) Taking this into consideration, it appears that M1 is a better candidate than M2 for reducing flow induced vibrations.

Finally, we note that this analysis is not complete in two respects: an accurate representation of the frequency spectra of the flow is lacking. This is because LES was used for the analysis. This can be overcome by using DNS. However, for the complicated geometries investigated here DNS may be prohibitively expensive. Secondly, accurate and reliable dynamic calculations of the response of the actuator arm to the flow is missing. This may be overcome by performing coupled fluid-structure interaction calculations.

References

- [1] S. D. Abrahamson, John Eaton, and D. J. Koga. The flow between shrouded co-rotating disks. *Physics of Fluids*, 1(2):241–251, 1989.
- [2] C. J. Chang, J. A. C. Humphrey, and R. Grief. Calculation of turbulent convection between corotating disks in axisymmetric enclosures. *International Journal of Heat and Mass Transfer*, 33(12):2701–2720, 1990.
- [3] M. Germano, U. Piomelli, P. Moin, and W. H. Cabot. A dynamic sub-grid scale eddy viscosity model. *Physics of Fluids*, A(3):1760–1765, 1991.
- [4] J. Girard, S. Abrahamson, and K. Uznanski. The effect of rotary arms on co-rotating disk flow. *ASME Journal of Fluids Engineering*, 117:259–272, 1995.
- [5] H. Gross. *Off-Track Vibrations of the Read-Write Heads in Hard Disk Drives*. PhD thesis, University of California, Berkeley, 2003.
- [6] Y. Hirono, T. Arisaka, N. Nishijima, T. Shimizu, S. Nakamura, and H. Masuda. Flow-induced vibration reduction in hdd by using a spoiler. *IEEE Transactions on Magnetics*, 40(4):3168–3170, 2004.
- [7] J. A. C. Humphrey, C. A. Schuler, and D. R. Webster. Unsteady laminar flow between a pair of disks corotating in a fixed cylindrical enclosure. *Physics of Fluids*, 7(6):1225–1240, 1995.
- [8] I. Iglesias and J. A. C. Humphrey. Two- and three-dimensional laminar flows between disks co-rotating in a fixed cylindrical enclosure. *International Journal for numerical methods in fluids*, 26:581–603, 1998.
- [9] R. Kaneko, S. Oguchi, and K. Hoshiya. Hydrodynamic characteristics in disk packs

- for magnetic storage. *Review of the Electrical Communication Laboratories, Nippon Telegraph and Telephone Public Corp., Japan*, 25:1325–1336, 1977.
- [10] H. Kazemi. *Mathematical Modeling of Flow-Induced Vibrations of Suspension-Head Units in Hard Disk Drives*. PhD thesis, University of Virginia, Charlottesville, 2004.
- [11] S. Kirpekar and David B. Bogy. A comparison of large eddy simulation models for numerical simulation of airflow in hard disk drives. *submitted to the ASME Journal of Fluids Engineering*, 2004.
- [12] P. J. Kundu. *Fluid Mechanics*. Academic Press, 1990.
- [13] E. Lennemann. Aerodynamic aspects of disk files. *IBM J. Res. Develop*, pages 480–488, 1974.
- [14] R. Mittal and P. Moin. Suitability of upwind-biased finite difference schemes for large-eddy simulation of turbulent flows. *AIAA Journal*, 38:1415–1417.
- [15] S. Nakamura, S. Wakatsuki, T. Haruhide, S. Saegusa, and Y. Hirono. Flow-induced vibration of head gimbal assembly. *IEEE Transactions on Magnetics*, 40(4):3198–3200, 2004.
- [16] E. Y. K. Ng and Z. Y. Liu. Prediction of unobstructed flow for co-rotating multi disk drive in an enclosure. *International Journal for numerical methods in fluids*, 35:519–531, 2001.
- [17] C. A. Schuler, W. Usry, B. Weber, J. A. C. Humphrey, and R. Grief. On the flow in the unobstructed space between shrouded corotating disks. *Physics of Fluids A* 2, 10:1760–1770, 1990.

- [18] H. Shimizu, T. Shimizu, M. Tokuyama, H. Masuda, and S. Nakamura. Numerical simulation of positioning error caused by air-flow-induced vibration of head gimbals assembly in hard disk drive. *IEEE Transactions on Magnetics*, 39(2):806–811, 2003.
- [19] H. Shimizu, M. Tokuyama, S. Imai, S. Nakamura, and K. Sakai. Study of aerodynamic characteristics in hard disk drives by numerical simulation. *IEEE Transactions on Magnetics*, 37(2):831–836, 2001.
- [20] H Song, M. Damodaran, and Q. Y. Ng. Simulation of flow field and particle trajectories in hard disk drive enclosures. *High Performance Computation for Engineered Systems (HPCES)*, Jan 2004.
- [21] H. Suzuki and J. A. C. Humphrey. Flow past large obstructions between corotating disks in fixed cylindrical enclosures. *ASME Journal of Fluids Engineering*, 119:499–505, 1997.
- [22] M. Tatewaki, N. Tsuda, and T. Maruyama. A numerical simulation of unsteady airflow in hdds. *FUJITSU Sci. Tech. J.*, 37(2):227–235, 2001.
- [23] N. Tsuda, H. Kobutera, M. Tatewaki, S. Noda, M. Hashiguchi, and T. Maruyama. Unsteady analysis and experimental verification of the aerodynamic vibration mechanism of hdd arms. *IEEE Transactions on Magnetics*, 39(2):819–825, 2003.
- [24] H. M. Tzeng and J. A. C. Humphrey. Corotating disk flow in an axisymmetric enclosure with and without a bluff body. *International Journal of Heat and Fluid Flow*, 12:194–201, 1991.
- [25] W. R. Usry, J. A. C. Humphrey, and R. Grief. Unsteady flow in the unobstructed space between disks corotating in a cylindrical enclosure. *ASME Journal of Fluids Engineering*, 115:620–626, 1993.

- [26] J. P. Van doormaal and G. D. Raithby. Enhancements of the simple method incompressible fluid flows. *Numerical Heat Transfer*, 7:147–163, 1984.
- [27] R. Wood, J Miles, and T. Olson. Recording technologies for terabit per square inch systems. *IEEE Transactions on Magnetics*, 38(4):1711–1718, 2002.
- [28] Y. Yamaguchi, A. A. Talukder, T. Shibuya, and M. Tokuyama. Air flow around a magnetic head slider suspension and its effects on the slider flying height fluctuations. *IEEE Transactions on Magnetics*, 26(5):2430–2432, 1990.

5 Tables

Table 1: Geometry data

Number of disks	2
Number of e-block arms	1
Number of base plates	2
Number of suspensions	2
Number of sliders	2
Spacing between disks (mm)	2.2
Disk diameter (mm)	76.2
Width of shroud gap (mm)	1
Length of actuator (mm)	45
Length of e-block arm (mm)	32.5
Length of base plate (mm)	6.5
Length of suspension (mm)	11.1
Thickness of e-block arm (mm)	0.8
Thickness of base plate (mm)	0.3
Thickness of suspension (mm)	0.1
Dimensions of slider (mm)	$1 \times 0.8 \times 0.3$
Number of weight saving holes in e-block arm	2

Table 2: Model specific geometry data, M1

Thickness of blocking plate (mm)	0.8
Angular dimension of blocking plate (degrees)	180
Radial dimension of blocking plate (mm)	16.25

Table 3: Model specific geometry data, M2

Thickness of downstream spoiler (mm)	1.6
Maximum width of downstream spoiler (mm)	2.65
Length of downstream spoiler (mm)	20.75

]

Table 4: Model specific geometry data, M3

Thickness of upstream spoiler (mm)	1.4
Maximum width of upstream spoiler (mm)	8
Length of upstream spoiler (mm)	17.5

Table 5: CFD modeling information

Governing equations	Filtered Navier Stokes equations
Solution algorithm	SIMPLEC [26]
Large eddy simulation model	Algebraic dynamic [3]
Type of LES filter	Top-hat (variable width)
Temporal differencing scheme	Implicit Euler
Spatial differencing scheme (convective term)	Central differencing
Time step (seconds)	2.0×10^{-5}
Number of time steps	2400
Corresponding number of disk rotations	8
Initial conditions	Steady k- ϵ solution

Table 6: Boundary conditions

Disks	Rigid rotating walls, no slip
Shroud	Rigid wall, no slip
Shroud gap	Axial symmetry (zero normal gradient)
Other top and bottom surfaces of computational volume	Axial symmetry (zero normal gradient)
Hub/base of e-block arm	Fixed (similar to a cantilever)
Slider-disk interface	Slider slips on disk No cells between slider and disk
All structural interfaces (e.g. suspension+slider, e-block arm+base plate)	Rigidly joined (i.e. no dimple)
All fluid-structure surfaces	Coupled for pressure and shear stress

Table 7: Grid information

	M0	M1	M2	M3
Type of mesh	unstructured, quad-dominant	←	←	←
Number of vols.	1,025,772	872,284	890,532	895,769
Max. cell vol. (mm ³)	8.996×10^{-2}	9.521×10^{-2}	9.436×10^{-2}	9.390×10^{-2}
Min. cell vol. (mm ³)	3.433×10^{-5}	3.315×10^{-5}	5.836×10^{-5}	6.855×10^{-5}
Avg. cell vol. (mm ³)	1.179×10^{-2}	1.243×10^{-2}	1.442×10^{-2}	1.571×10^{-2}
Avg. grid res. (mm)	0.2276	0.2316	0.2434	0.2504

Table 8: Common Legend for Figures in the paper

M0	Full Line	Original Simulation
M1	Dashed Line	Blocking Plate
M2	Dotted Line	Downstream Spoiler
M3	Dash-Dotted Line	Upstream Spoiler

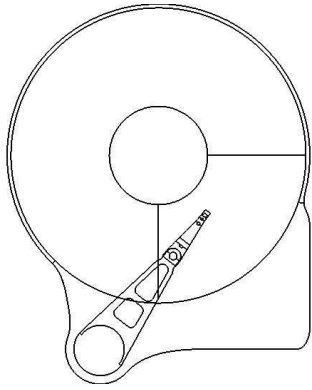


Figure 1: Top view of M0: original simulation

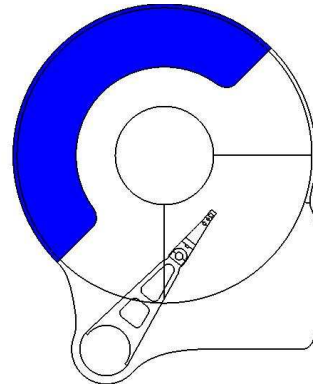


Figure 2: Top view of M1: blocking plate

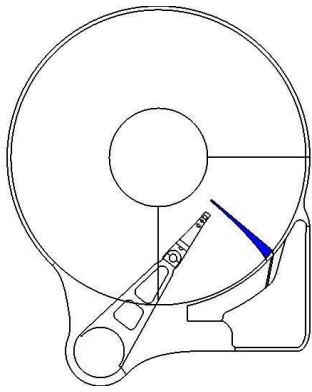


Figure 3: Top view of M2: downstream spoiler

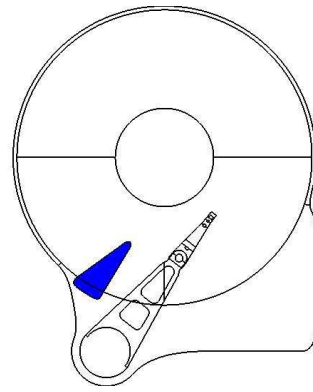


Figure 4: Top view of M3: upstream spoiler

6 Figures

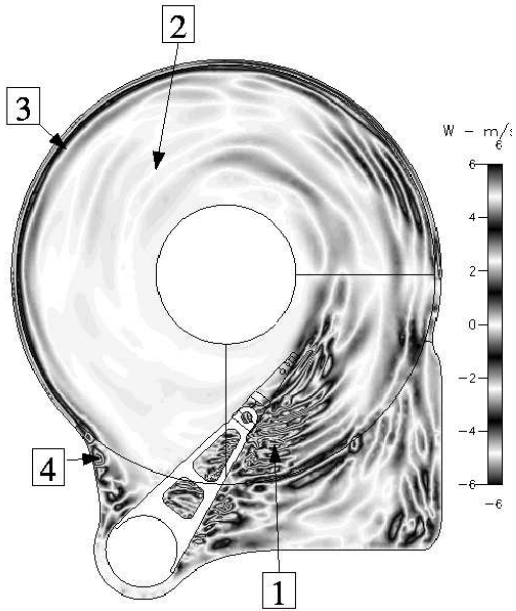


Figure 5: M0: Snapshot of turbulent field in the drive. Plot of axial velocity component on the midplane

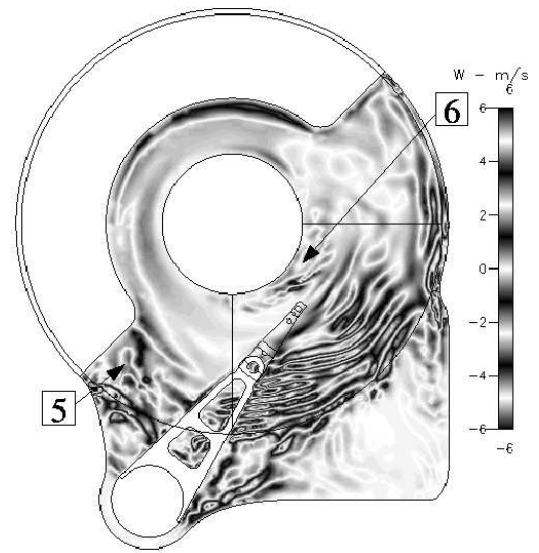


Figure 6: M1: Snapshot of turbulent field in the drive. Plot of axial velocity component on the midplane

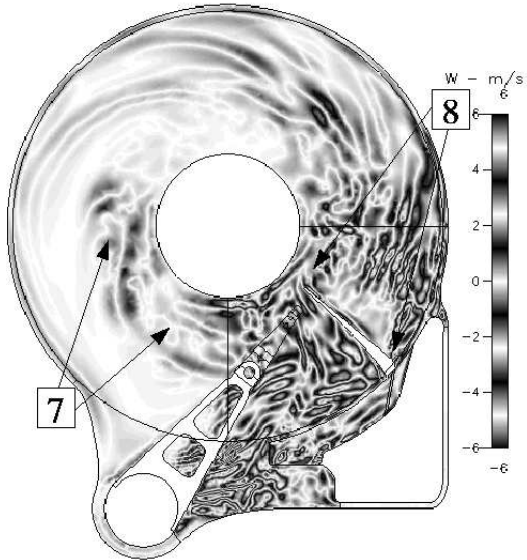


Figure 7: M2: Snapshot of turbulent field in the drive. Plot of axial velocity component on the midplane

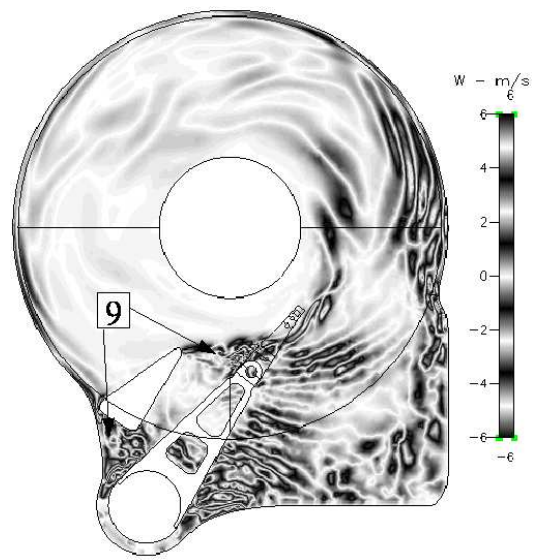


Figure 8: M3: Snapshot of turbulent field in the drive. Plot of axial velocity component on the midplane

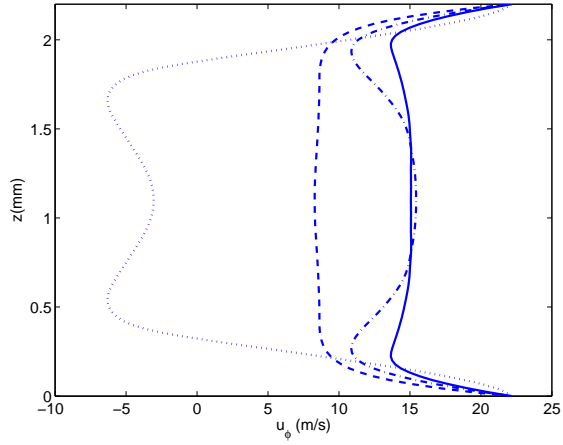


Figure 9: Inter-disk azimuthal velocity profile, at 340° from origin, i.e. in the wake (See Table 8 for legend)

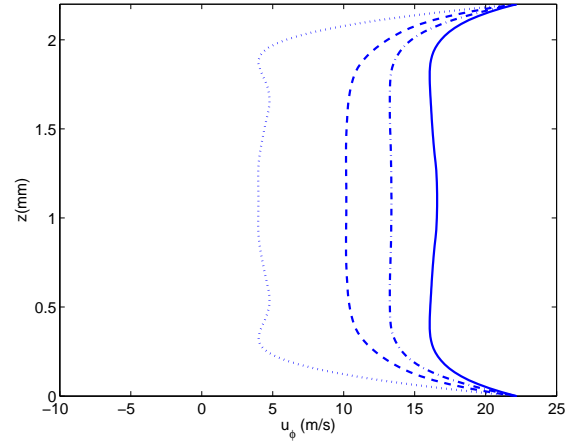


Figure 10: Inter-disk azimuthal velocity profile, at 45° from origin (See Table 8 for legend)

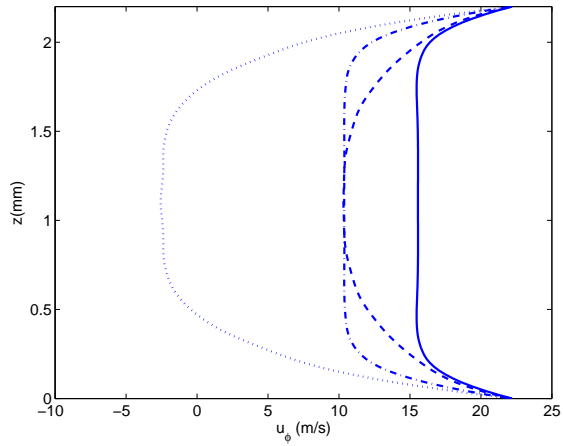


Figure 11: Inter-disk azimuthal velocity profile, at 135° from origin (See Table 8 for legend)

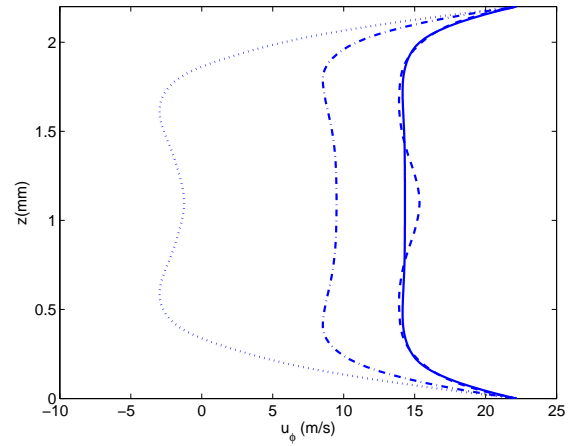


Figure 12: Inter-disk azimuthal velocity profile, at 225° from origin (See Table 8 for legend)

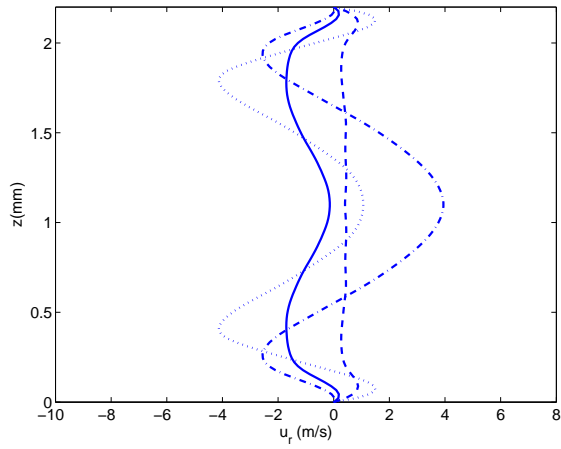


Figure 13: Inter-disk radial velocity profile, at 340° from origin, i.e. in the wake (See Table 8 for legend)

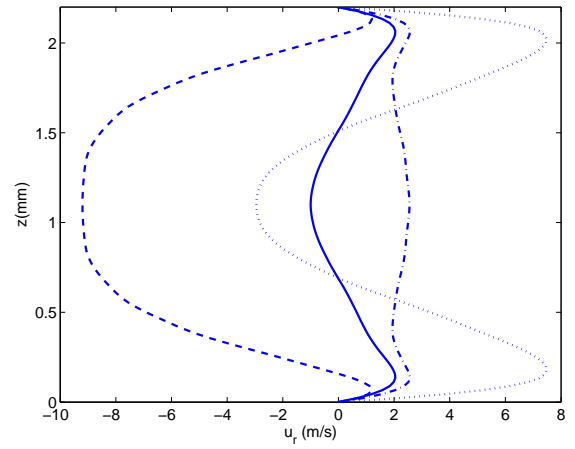


Figure 14: Inter-disk radial velocity profile, at 45° from origin (See Table 8 for legend)

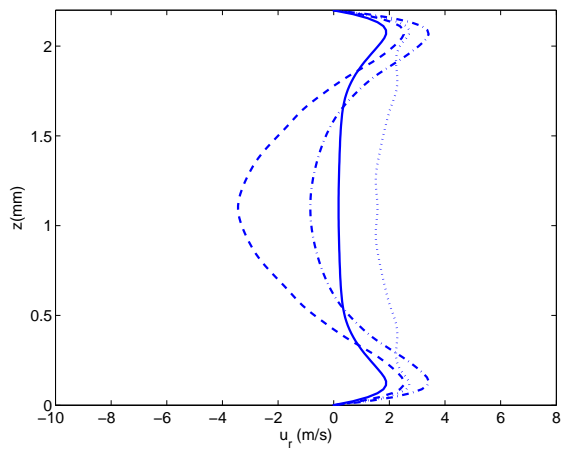


Figure 15: Inter-disk radial velocity profile, at 135° from origin (See Table 8 for legend)

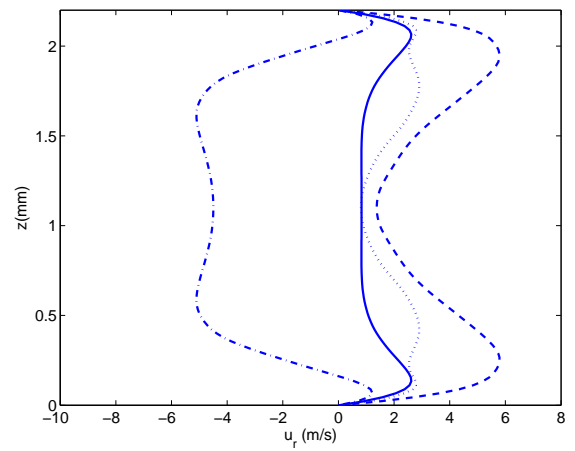


Figure 16: Inter-disk radial velocity profile, at 225° from origin (See Table 8 for legend)

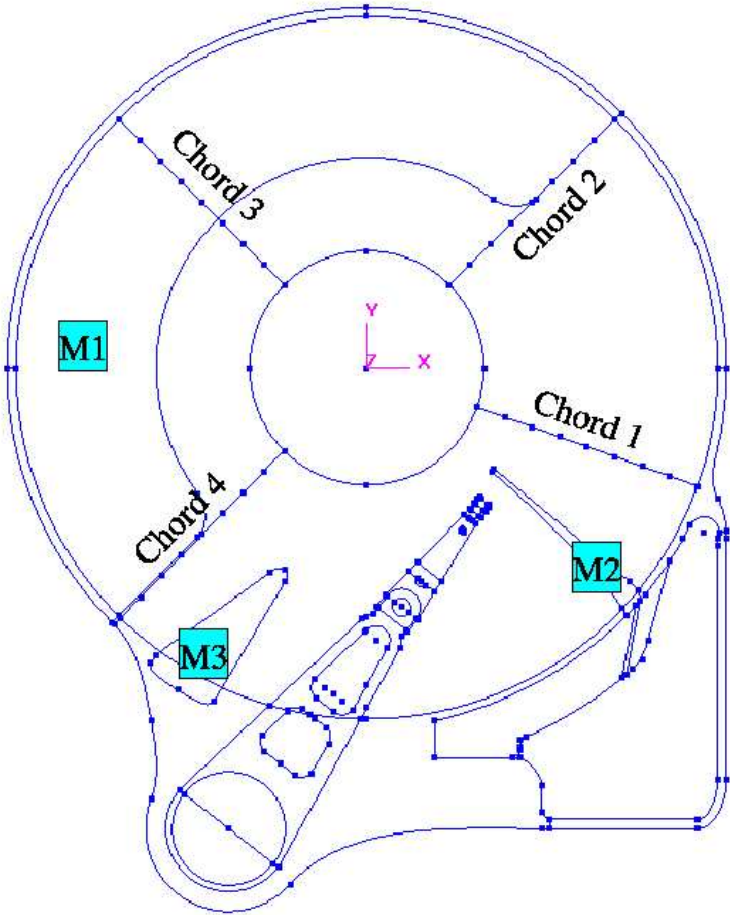


Figure 17: Chord locations for calculation of turbulence intensity

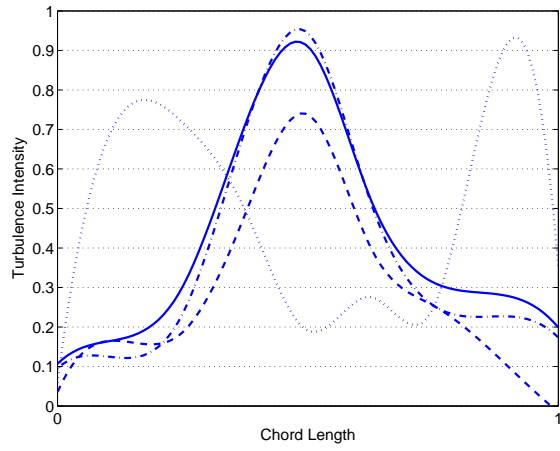


Figure 18: Turbulence Intensity along chord 1 (See Table 8 for legend)

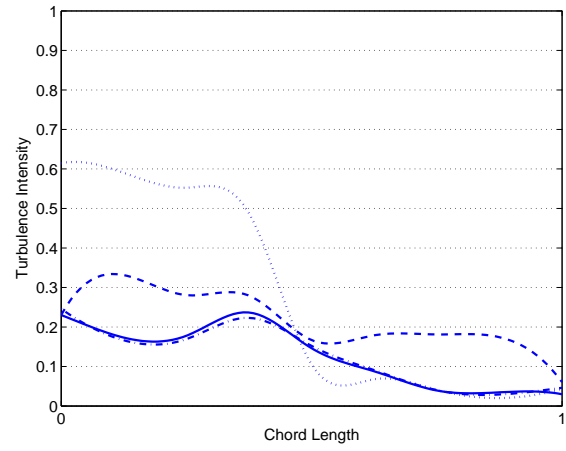


Figure 19: Turbulence Intensity along chord 2 (See Table 8 for legend)

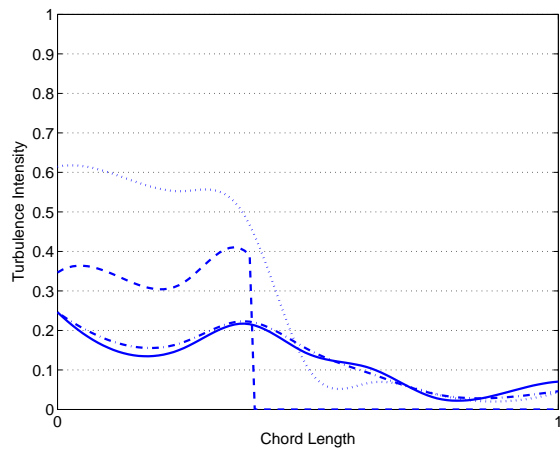


Figure 20: Turbulence Intensity along chord 3 (See Table 8 for legend)

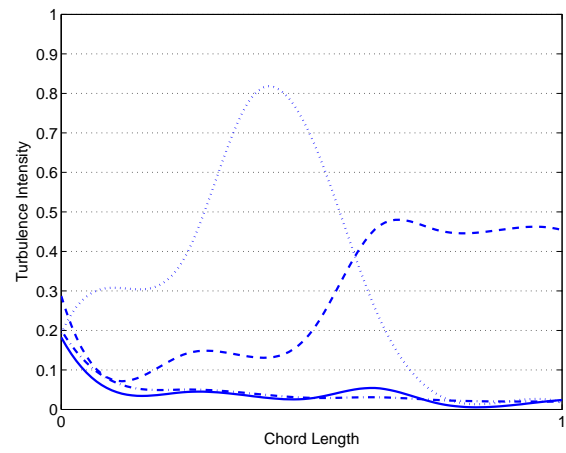


Figure 21: Turbulence Intensity along chord 4 (See Table 8 for legend)

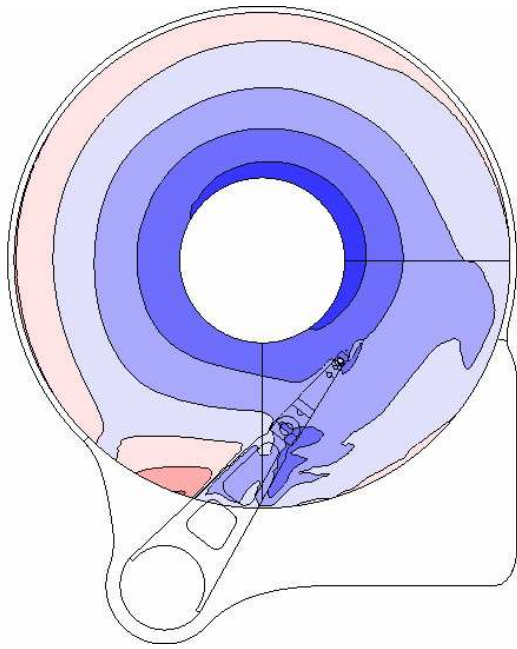


Figure 22: M0: Contours of the instantaneous pressure field acting on the top disk

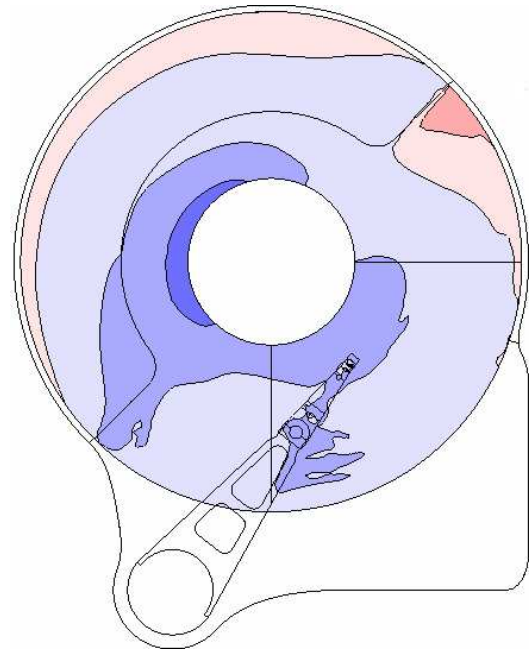


Figure 23: M1: Contours of the instantaneous pressure field acting on the top disk

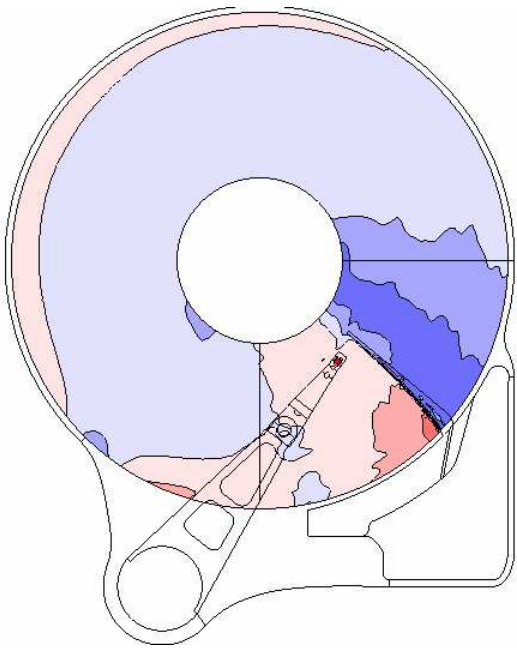


Figure 24: M2: Contours of the instantaneous pressure field acting on the top disk

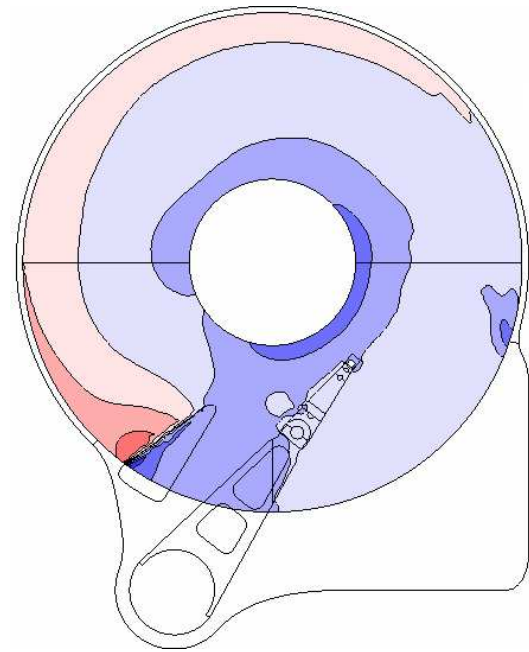


Figure 25: M3: Contours of the instantaneous pressure field acting on the top disk

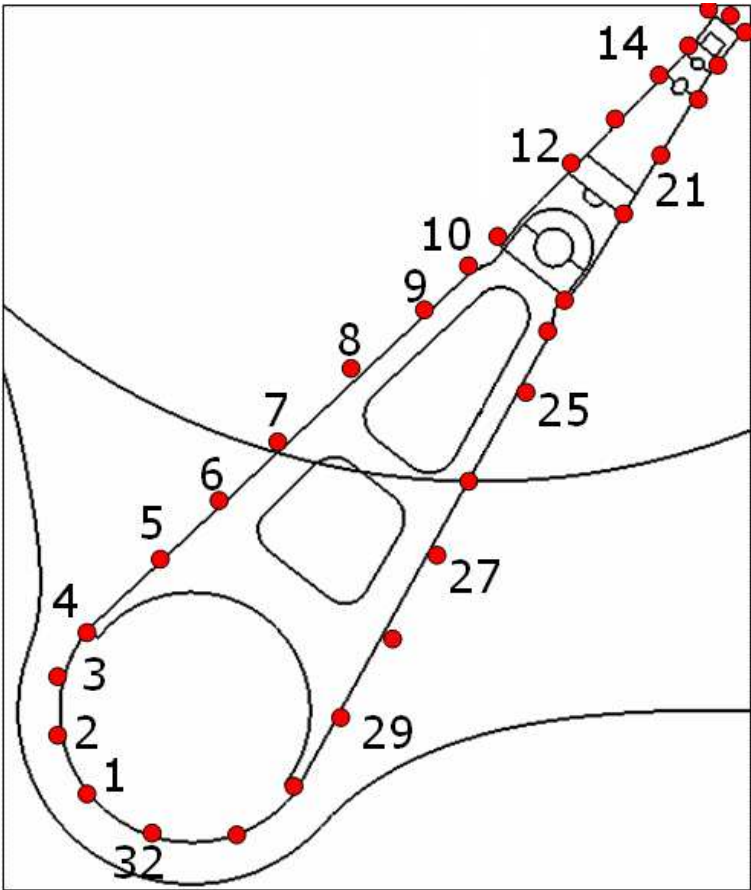


Figure 26: Location of points along actuator face for which velocity and pressure data is reported

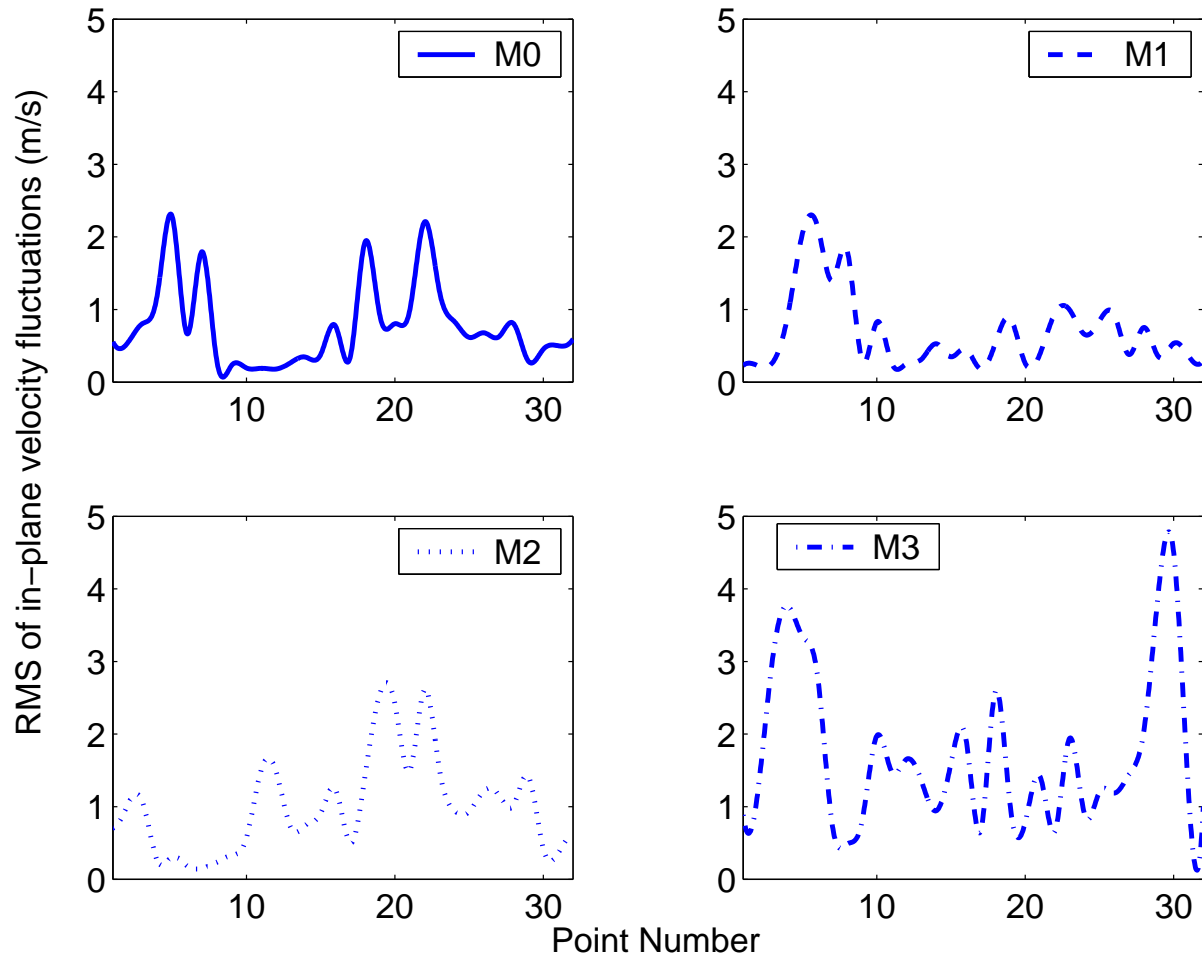


Figure 27: RMS fluctuation of in-plane velocity fluctuations (See Table 8 for legend)

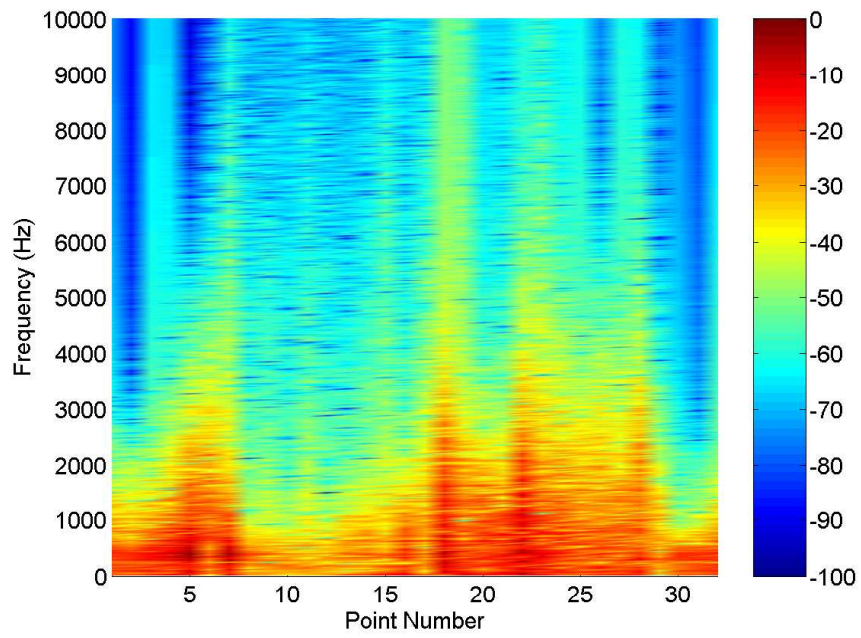


Figure 28: M0: Frequency Spectra of in-plane velocity fluctuations for data points 1-32

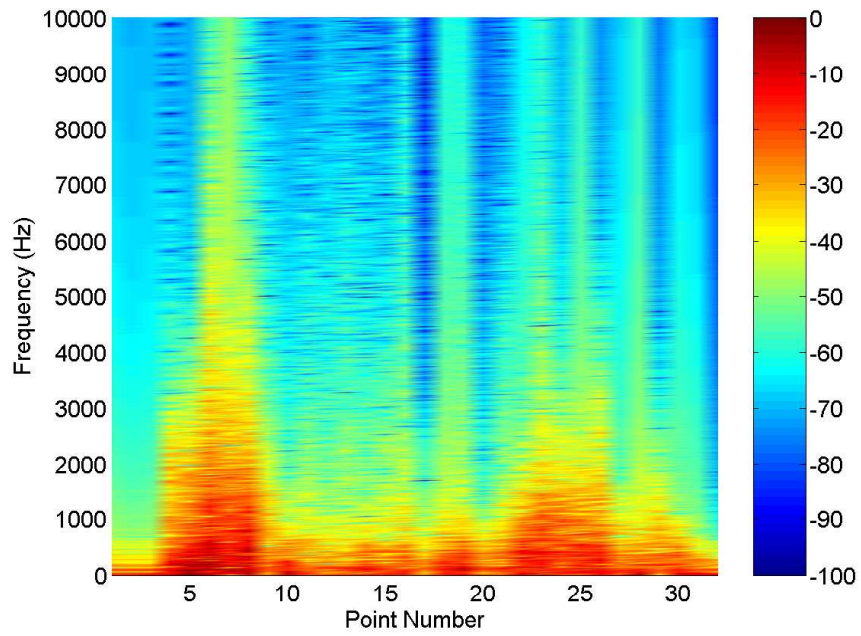


Figure 29: M1: Frequency Spectra of in-plane velocity fluctuations for data points 1-32

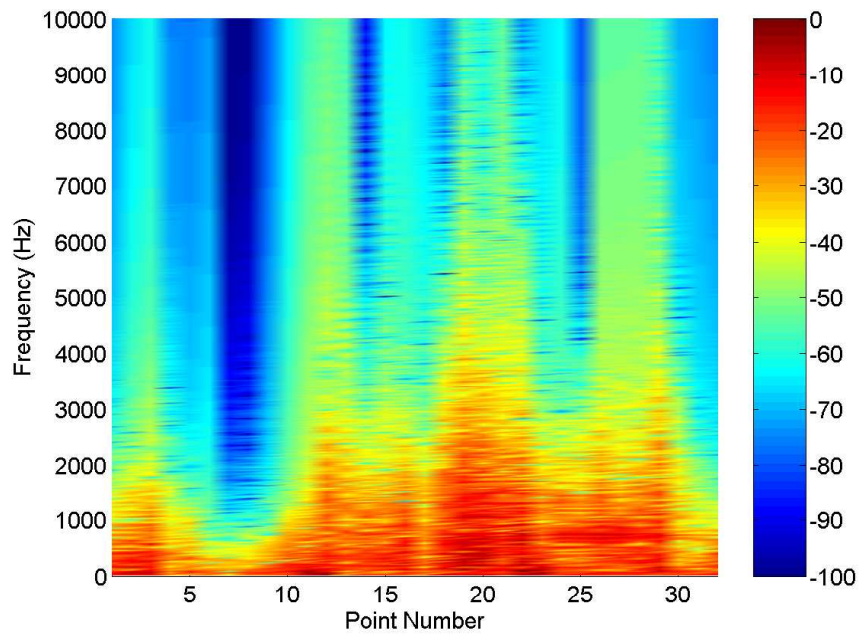


Figure 30: M2: Frequency Spectra of in-plane velocity fluctuations for data points 1-32

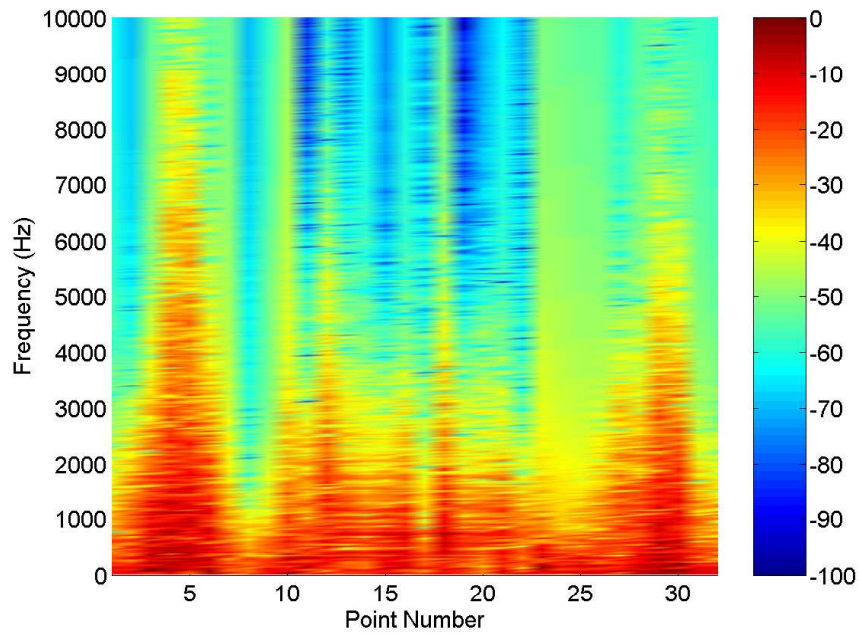


Figure 31: M3: Frequency Spectra of in-plane velocity fluctuations for data points 1-32

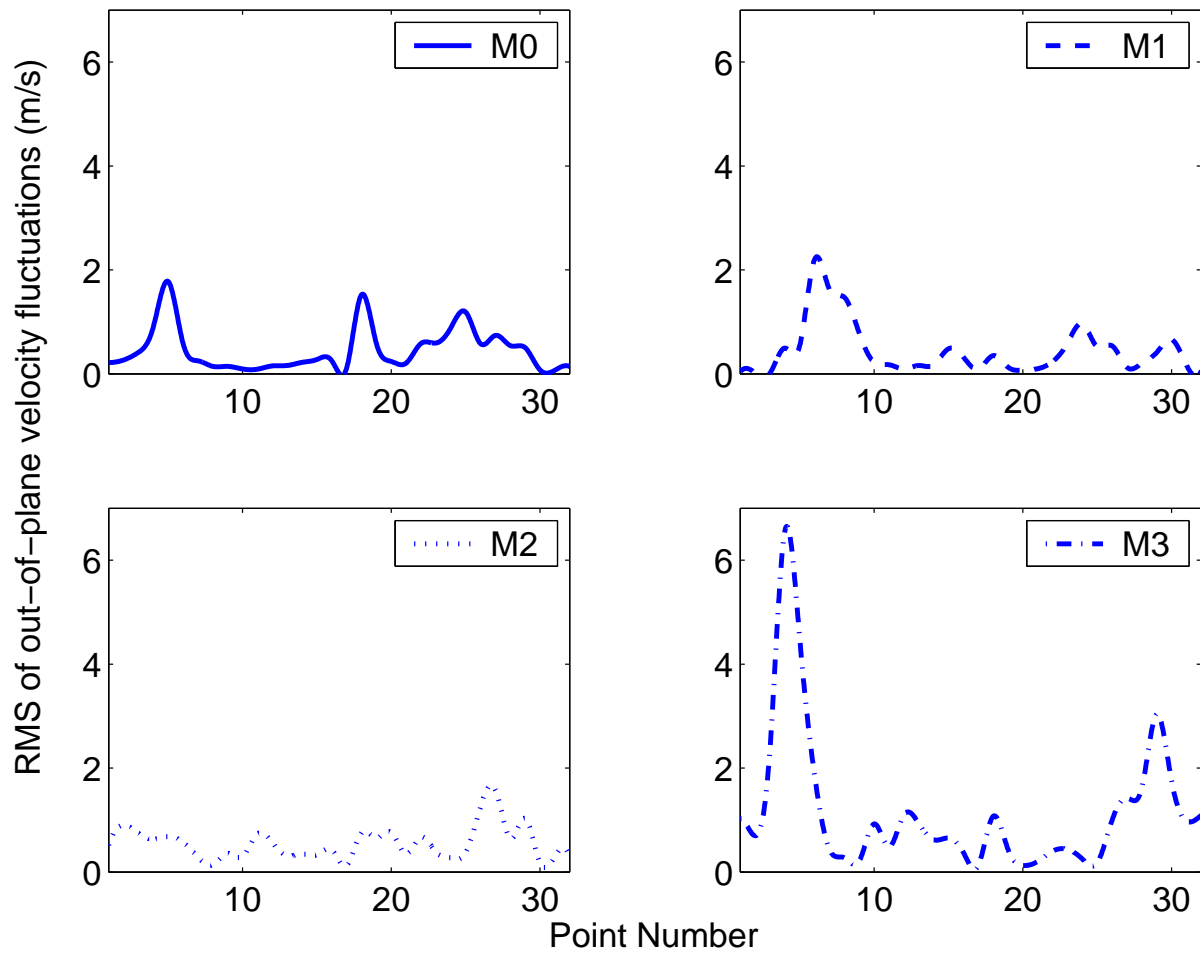


Figure 32: RMS fluctuation of out-of-plane velocity fluctuations (See Table 8 for legend)

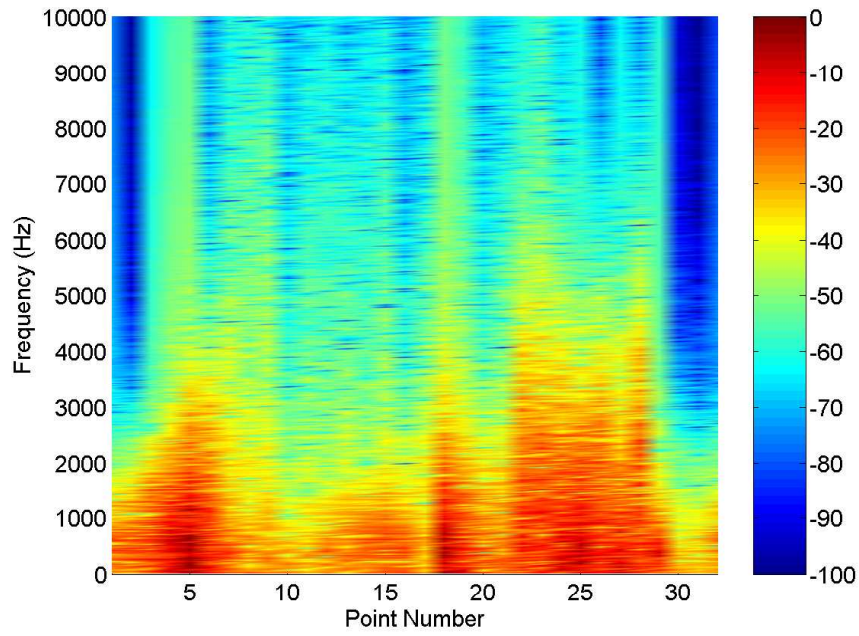


Figure 33: M0: Frequency Spectra of out-of-plane velocity fluctuations for data points 1-32

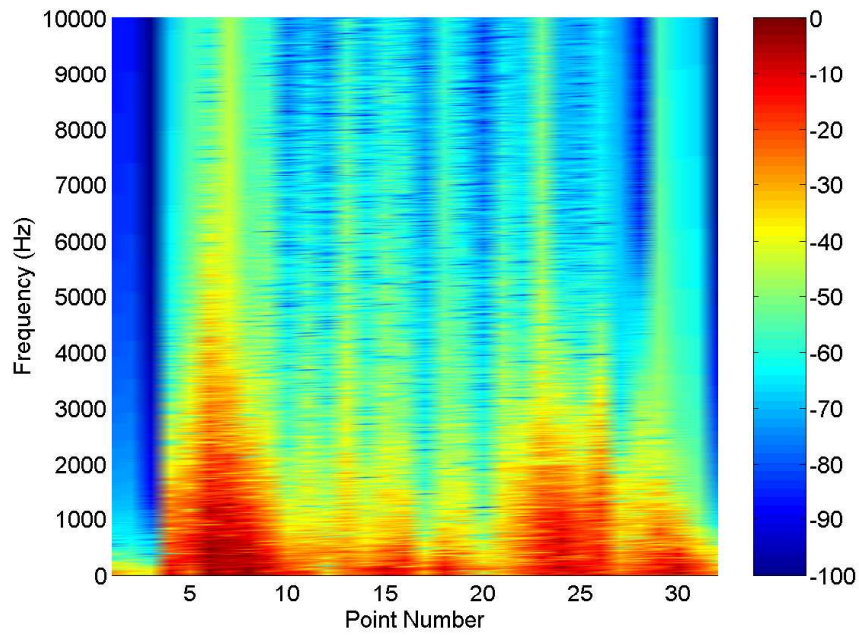


Figure 34: M1: Frequency Spectra of out-of-plane velocity fluctuations for data points 1-32

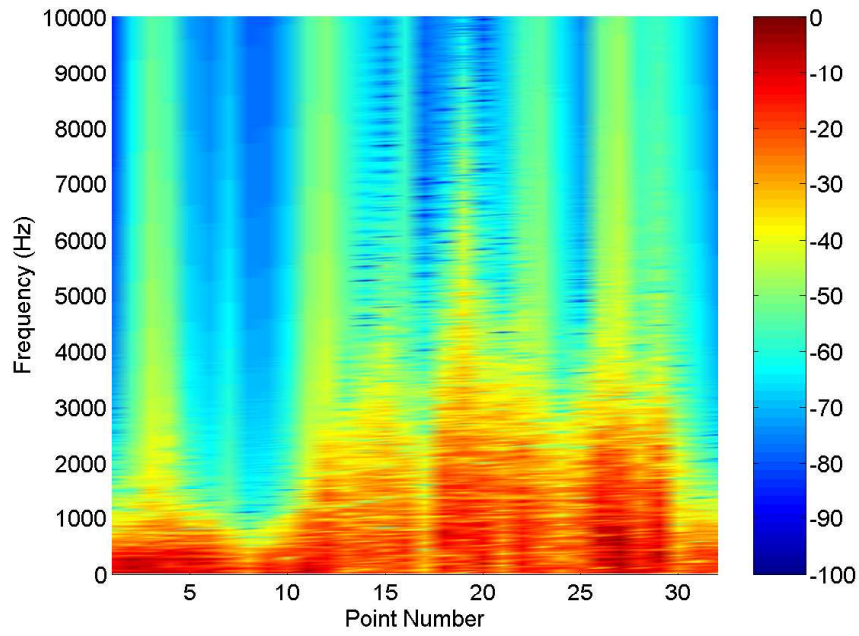


Figure 35: M2: Frequency Spectra of out-of-plane velocity fluctuations for data points 1-32

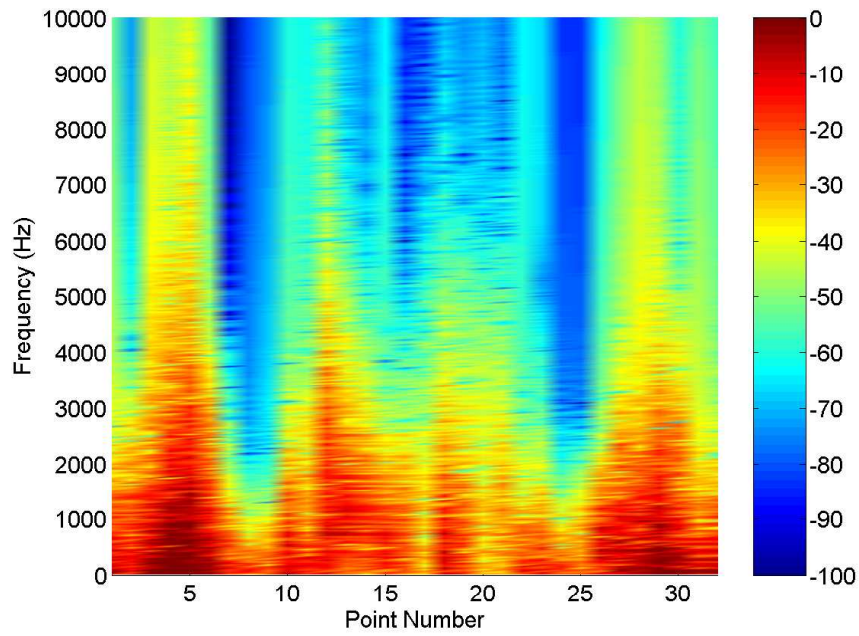


Figure 36: M3: Frequency Spectra of out-of-plane velocity fluctuations for data points 1-32

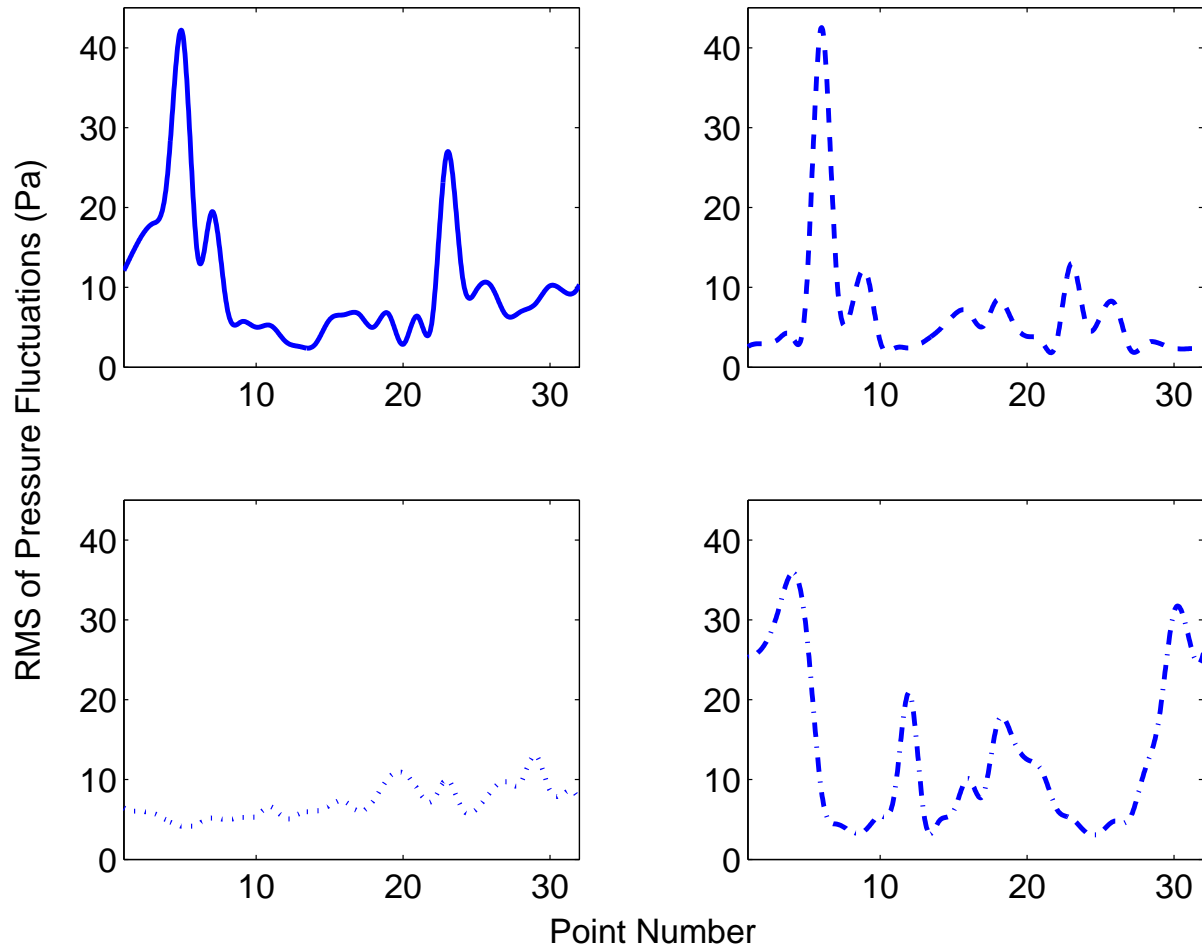


Figure 37: RMS fluctuations of Pressure (See Table 8 for legend)

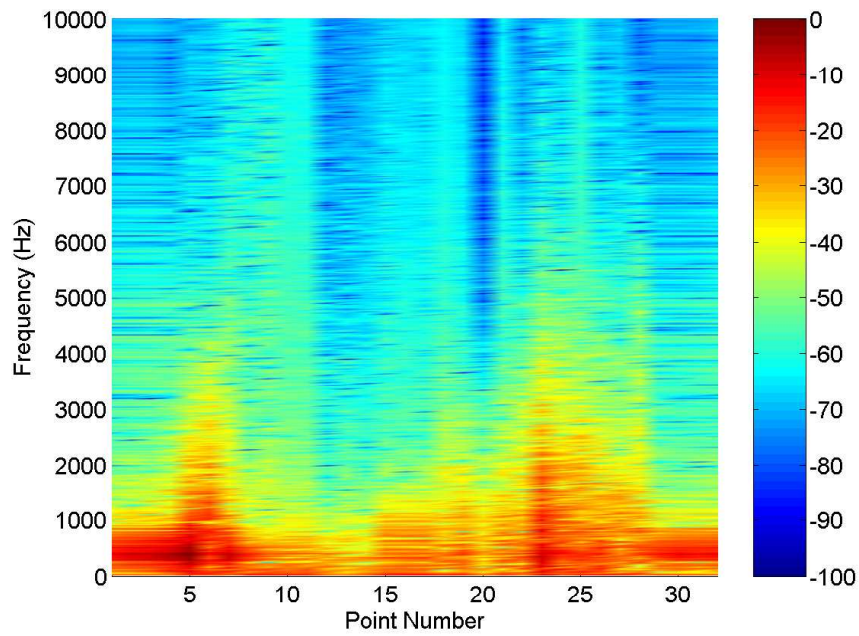


Figure 38: M0: Frequency Spectra of pressure fluctuations for data points 1-32

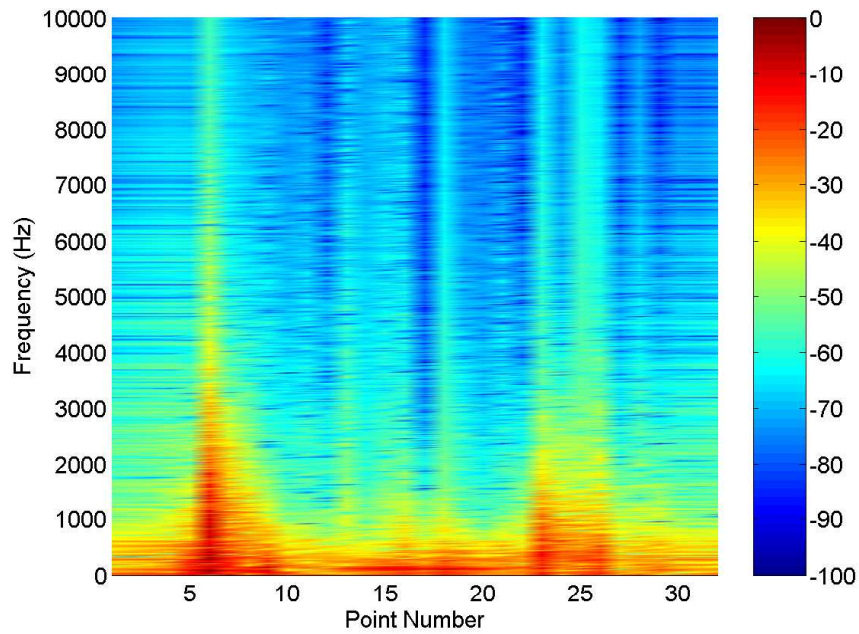


Figure 39: M1: Frequency Spectra of pressure fluctuations for data points 1-32

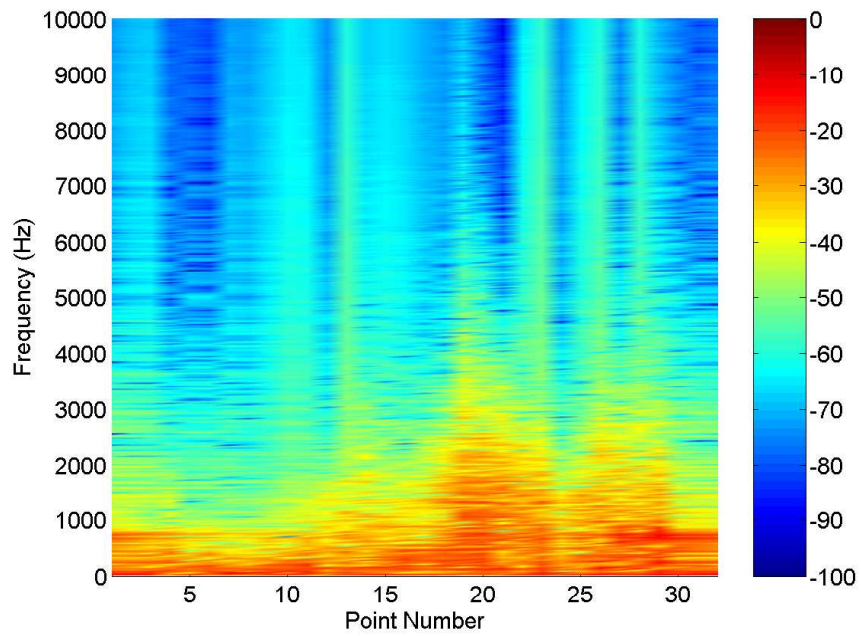


Figure 40: M2: Frequency Spectra of pressure fluctuations for data points 1-32

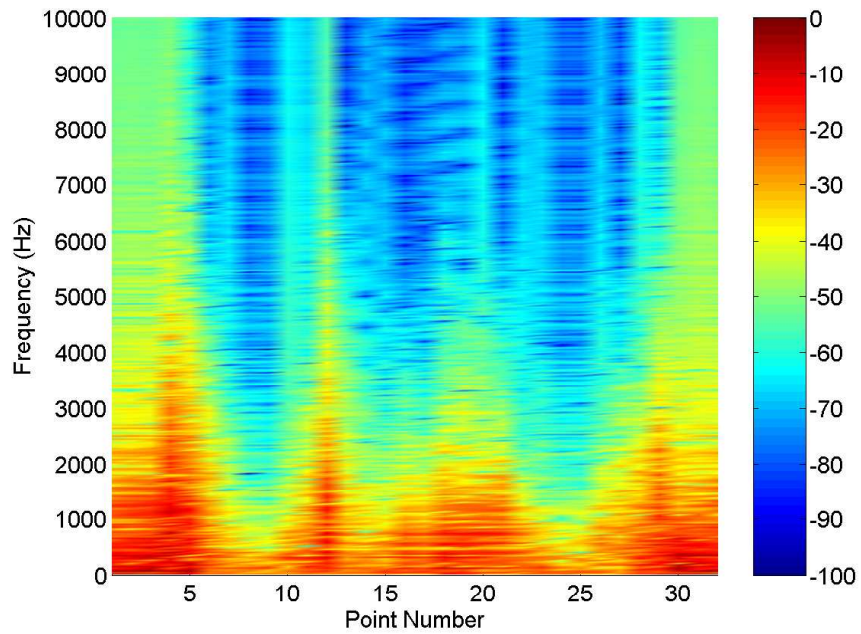


Figure 41: M3: Frequency Spectra of pressure fluctuations for data points 1-32

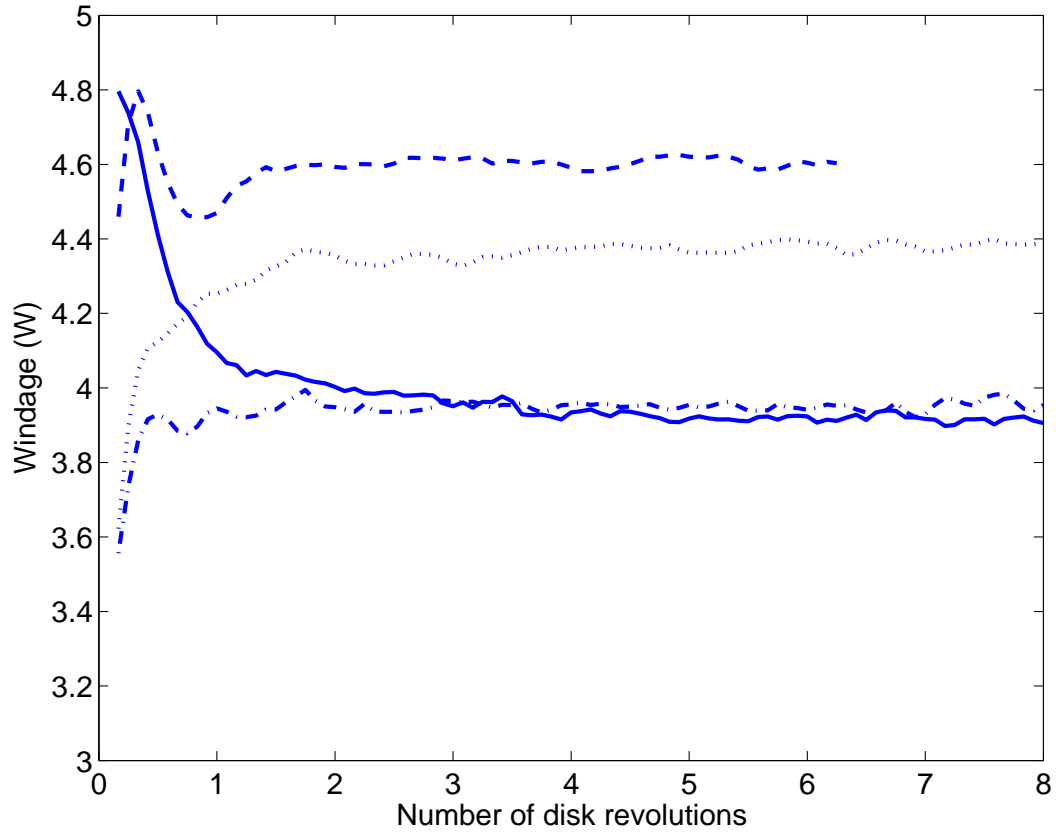


Figure 42: Windage loss at disks (See Table 8 for legend)